Spatially Resolved MR-Compatible Doppler Ultrasound: Proof of Concept for Triggering of Diagnostic Quality Cardiovascular MRI for Function and Flow Quantification at 3T.

Lindsey Alexandra Crowe, Gibran Manasseh, Aneta Chmielewski, Anne-Lise Hachulla, Daniel Speicher, Andreas Greiser, Hajo Müller, Thomas de Perrot, Jean-Paul Vallée, and Rares Salomir

Abstract*—*Objective: **We demonstrate the use of a magnetic-resonance (MR)-compatible ultrasound (US) imaging probe using spatially resolved Doppler for diagnostic quality cardiovascular MR imaging (MRI) as an initial step toward hybrid US/MR fetal imaging. *Methods:* A newly developed technology for a dedicated MR-compatible phased array ultrasound-imaging probe acquired pulsed color Doppler carotid images, which were converted in near-real time to a trigger signal for cardiac cine and flow quantification MRI. Ultrasound and MR data acquired simultaneously were interference free. Conventional electrocardiogram (ECG) and the proposed spatially resolved Doppler triggering were compared in 10 healthy volunteers. A synthetic "false-triggered" image was retrospectively processed using metric optimized gating (MOG). Images were scored by expert readers, and sharpness, cardiac function and aortic flow were quantified. Four-dimensional (4-D) flow (two volunteers) showed feasibility of Doppler triggering over a long acquisition time. *Results:* Imaging modalities were compatible. US probe positioning was stable and comfortable. Image quality scores and quantified sharpness were statistically equal for Doppler- and ECG-triggering ($p = 1.00$). ECG-, Doppler-triggered, and MOG ejection fractions were equivalent ($p = 1.00$), with false-triggered values significantly lower ($p < 0.0005$). Aortic flow showed no difference between ECG- and Doppler-triggered and MOG ($p > 0.05$). 4-D flow quantification gave consistent results between ECG and Doppler triggering. *Conclusion:* We report interference-free pulsed color Doppler ultrasound during MR data acquisition. Cardiovascular MRI of diagnostic quality was successfully obtained with pulsed color Doppler triggering. *Significance:* The hardware platform could further enable advanced free-breathing cardiac imaging. Doppler ultrasound triggering is applicable where ECG is compromised due to pathology or interference at higher magnetic fields, and where direct ECG is impossible, i.e., fetal imaging.**

***Index Terms*—Cardiac function, ECG, Doppler ultrasound, metric optimized gating, MRI.**

Manuscript received July 7, 2017; revised September 18, 2017; accepted October 7, 2017. Date of publication October 18, 2017; date of current version January 18, 2018. This work was supported in part by the Centre for Biomedical Imaging (CIBM) of EPFL, in part by the University of Geneva, and in part by the University Hospitals of Geneva and Lausanne via the Swiss National Foundation under R'Equip Grant 326030_150816 and a DISIM departmental start-up Grant. *(Corresponding author: Lindsey Alexandra Crowe.)*

L. A. Crowe is with the Service of Radiology, Geneva University Hospitals, Rue-Gabrielle-Perret-Gentil 4, Geneva 1205, Switzerland (e-mail: lindsey.crowe@unige.ch).

G. Manasseh is with the Image Guided Interventions Laboratory, Faculty of Medicine, University of Geneva.

A. Chmielewski is with the Division of Physiology and Experimental Medicine, Hospital for Sick Children.

A.-L. Hachulla, T. de Perrot, and J.-P. Vallée are with the Service of Radiology, Faculty of Medicine, Geneva University Hospitals.

D. Speicher is with the Fraunhofer Institute for Biomedical Engineering (IBMT).

A. Greiser is with the Siemens Healthcare.

H. Müller is with the Unit of Echocardiography, Service of Cardiology, Faculty of Medicine, Geneva University Hospitals.

R. Salomir is with the Image Guided Interventions Laboratory, Faculty of Medicine, University of Geneva, and also with the Service of Radiology, Faculty of Medicine, Geneva University Hospitals.

This paper has supplementary downloadable material available at http://ieeexplore.ieee.org, provided by the author.

Digital Object Identifier 10.1109/TBME.2017.2764111

List of abbreviations

MR(I)	Magnetic Resonance Imaging
US	Ultrasound
ECG	Electrocardiogram
MOG	Metric Optimized Gating
HIFU	High Intensity Focused Ultrasound
FOV	Field of View
RF	Radio-Frequency
ROI	Region Of Interest
2C, 4C, SA	2-Chamber, 4-Chamber, Short Axis
TrueFISP	True Fast Imaging with Steady-state Precession
TE	Echo Time
TR	Repetition Time
PC	Phase Contrast
FLASH	Fast Low Angle Shot
DICOM	Digital Imaging and Communications in Medicine
EF	Ejection Fraction
EDV	End-diastolic Volume
ESV	End-systolic Volume
LV	Left Ventricle

Supplementary Data and Movies

A: MOVIE	Illustration of pulsed color Doppler image.
B: MOVIE	Recording of the Doppler signal in one volunteer with significant carotid motion during respiration.
C: DATA	Position of US probe and temperature sensor on an MR image and graph showing no heating of the transducer surface measured using an MR-compatible fluoroptic fibre.
D: MOVIE	Cardiac cine movies: First row, 2 chamber; Second row, 4 chamber; Third row, short axis: Columns ECG triggered, Doppler triggered, false trigger, MOG reconstruction.
E&F: MOVIES	4D Flow reconstructions with Doppler- and ECG triggering.

I. Introduction

OVER the last decade, the possibility of coupling MRI and Ultrasound (US) imaging in order to exploit the strength of both imaging modalities has been proposed by various groups. Technical feasibility in phantoms has been reported [1], and other hybrid acquisition systems have also been introduced more recently [2]–[5]. This technologic integration is interesting as both modalities are non-invasive, but a major obstacle was the mutual electromagnetic interference. Simultaneous MR and US imaging has been used for guiding biopsy (for needle tracking and confirmation of needle placement at 0.5 and 3T [6]) and for real-time methods for HIFU (High Intensity Focused Ultrasound) guidance [1], [2], though few studies exist for dynamic imaging and the cardiovascular system [1]. A potential application for hybrid US/MR imaging, not yet validated on human subjects, is fetal cardiac [7] which has only been shown in an animal model [8]. In utero diagnosis of congenital malformation is of vital importance for medical care, pre-surgical planning and the impact on postnatal outcome [9]–[11].

Functional cardiac MRI scans performed in clinical routine use ECG signals for triggering the acquisition. With increasing field strength, interference with ECG detection has become a more significant problem [12]. Additionally, signal complications due to obesity or pathology (for example with pericardial fluid or scaring), or the complete absence of direct ECG for fetal imaging, mean that a new triggering method is sought [13]. A study by Rubin *et al*. [14] showed 1.5T MRI images acquired with a mono-element acoustic transducer using a direct temporal signal from the US. As this was pulsed, but not spatially resolved Doppler, it was not based on topology and therefore could be subject to signal modulation due to local motion drift with respect to the direction of scanning.

Self-gating techniques [15]–[18] have also been reported for cardiovascular MRI, where part of the image data itself is used for triggering and motion correction, but these rely on modification of the acquisition sequence. These sequences are often based on a radial acquisition trajectory and possibly coupled with acceleration methods such as compressed sensing [19], thus leading to long postprocessing times. Fetal cardiac cine imaging post-processing techniques [7] or using highly accelerated dynamic MRI with retrospective motion correction and outlier rejection has been reported [20].

Another method of cardiac synchronization, retrospective processing using Metric Optimized Gating (MOG) [21]–[23], was proposed for cases where a reliable electrocardiogram is not obtainable. The acquisition used in this post-processing method is performed without a true input trigger signal and the acquired lines are retrospectively sorted by optimizing image metrics.

Aiming for US-guided MR imaging dedicated to fetal applications, we report here interference-free spatially resolved pulsed color Doppler acquired inside an MR magnet bore concurrently to MR scanner operation. To this purpose, a dedicated MR-compatible US imaging transducer was manufactured and validated for interference-free B-mode and pulsed color Doppler simultaneous to MR acquisition. As a step towards full ultrasound-controlled hybrid MRI of the heart, here we propose feasibility of triggering to carotid ultrasound. We used therefore directly the mechanical signal related to blood flow or tissue displacement, instead of electrical stimulation. MOG post-processing reconstruction, along with the 'false-triggered' acquired images it corrects, were included in the current study to provide a varied set of triggering and reconstruction methods as possible alternatives for cases with difficult ECG.

Finally, the feasibility of Doppler triggering for the rapidly expanding field of 4D flow [24], [25] was assessed. This provided comparison of the triggering methods during a longer acquisition time.

II. Methods

A. Acquisition: US Imaging and on Line Processing

Simultaneous real-time 2D US imaging was performed using a 7.5 MHz MRI compatible phased array transducer with 128 piezo ceramic elements. The transducer had a bandwidth of 6 MHz and an inter-element pitch of the linear array of 0.1 mm, 12.8 mm aperture, operated at frame rates of 15–50 images per second (depending on the field of view (FOV)). The sophisticated shielding concept of the 2 cm $\times$ 3.5 cm $\times$ 10.5 cm external housing, as well as the 8 m long multi coax cable, have been designed to minimize susceptibility artifacts and to avoid radio-frequency- (RF-) and gradient-switching interferences. The combined reactance of the array and the cable was canceled using miniature inductances embedded in the zero-insertion-force plug. As compared to the reference product (imaging probe P10.4, Siemens, Acuson Antares, Mountain View, CA) the real part of the impedance was augmented by approximately 10 Ohms due to the increased length of the cable. The geometry of materials used in the RF shielding of the US transducer prevented any electric contact between the conductive parts of the transducer and the volunteers' skin. To minimize elevational slice thickness, an acoustic lens made of rubber silicon was attached to the front side of the transducer, see Fig. 1(A). This layer also provided galvanic isolation between the electrical ground of the transducer and the volunteer's skin. The casing of the US transducer was 3D printed in acrylic resin (Paket VeroWhitePlus RGD835, Alphacam Swiss GmbH, Widnau, Switerland) and a non-magnetic metal layer was applied on its inner surface. This layer accurately

(A)

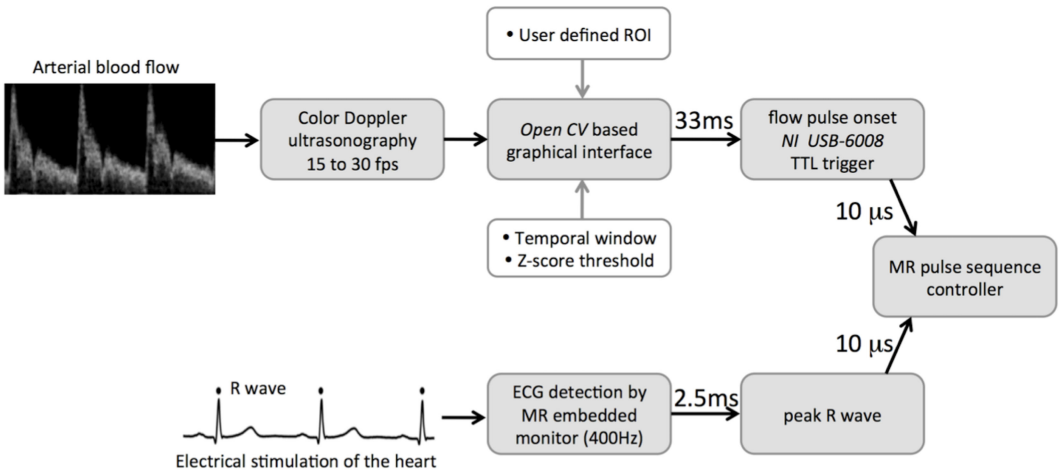

(B)

Fig. 1. (A) Setup showing ultrasound probe with shielded cable (face and side views) and the probe held in position. (B) Flow chart of data transfer. The spectral Doppler of arterial blood flow is provided to illustrate the periodicity comparison with ECG and the SNR, and leads to the pulsed color Doppler signal used in the method.

encompassed the border of the active matrix without electrical contact to the transducer and is further wired to the shielding mesh. The shielding mesh was in contact with the Faraday cage but is isolated from the electrical ground of the beamformer electronics and at no time was this in electrical contact with the patient. Experiments were performed in order to monitor the potential heating of the transducer using an MR-compatible fluoroptic fibre in contact with the surface during scanning. The transducer was positioned on the patient using an elastic belt, targeting the left common carotid artery, as shown in Fig. 1(A), which illustrates the ultrasound set up. The ultrasound scanner (Siemens ACUSON Antares, Siemens Healthcare, Mountain View, USA) was outside the Faraday cage with the probe passing through a waveguide. The EM shielding layer was placed in contact with the Faraday cage. This shielding is separated from the electrical ground of the US imager. The echoes were reconstructed using the built-in medical software. Main ultrasound acquisition parameters for the pulsed color Doppler were: frequency 5 MHz, peak transmit power −7 dB, velocity-encoding range (component parallel to the probe) 33 cm/s, field depth 4 cm, mechanical index 1; and for the background grayscale, parameters were: frequency 7.27 MHz, peak transmit power 35 dB, overall receiver gain 60 dB. The mechanical (MI) and thermal (TI) indices changed with the size and depth of the pulsed color Doppler region of interest, with MI found in the range 0.5–1.0 and TI in the range 0.7–1.0. When targeting the common carotid, typical values were MI 0.8 and TI 0.8. In harmonic mode gray scale imaging of background tissue, the TI decreased to 0.6 and the MI increased to 0.9.

Magnitude pulsed color Doppler images were exported in near real-time and analyzed by an external computer running a graphical interface based on Open CV libraries and driving a DAC board (USB-6008, National Instruments, Austin, TX) which generated the TTL triggers to the MR system, see Fig. 1(B) for details on signal flow chart. A user-defined polygon ROI was drawn in the image, larger than the vessel of interest, to include the vessel giving color signal and exclude other color signal in the rest of the image from other visible vessels. The signal conversion takes the integral of the color signal in that ROI while the B-mode background image is grayscale. The detection algorithm searched the relative contrast between red, green and blue layers. The detection of the yellow color of the Doppler peak was ensured by the algorithm selecting pixels that had the highest red or green component (yellow being a mix of red and green layers), and those that had the lowest possible blue component in order to exclude the grayscale background pixels. To achieved this, we computed a value $C = (R + G)/B$ where R, G and B are the pixel values of the 3 channel image with RGB color. This computation was in near-real time, for each captured ultrasound image and for each pixel in the ROI. An ROI pixel

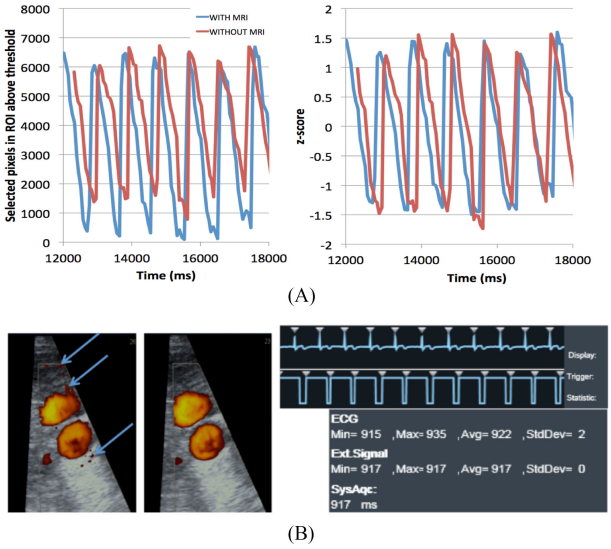

Fig. 2. (A) Extract of Doppler data: selected pixels in the ROI above threshold and corresponding z score sent to trigger with and without MRI running (note: separate acquisitions, therefore variations in the time scale can be expected). (B) Pulsed color Doppler image within the MR scanner showing small, negligible artifacts when the MRI is running (indicated by arrows) with and without MRI. Illustration of Doppler signal conversion and output to the MRI along with ECG and generated Doppler input signal from the common left carotid artery.

was considered as part of the vessel (contributive) if its value C was greater than a given threshold. The closer to the cardiac impulse in the arteries, the greater the Doppler signal and therefore the greater the number of contributive pixels. The number of all contributive pixels in the image was extracted and serially stored in a temporal vector. The most recent 100 sampling points in this temporal vector (i.e., a sliding window of 2 – 3 seconds) was used to calculate the standard score, also called z-score [26]. The value of z-score represents the distance between the actual raw value of the signal and the signal mean over the sliding window in units of the standard deviation. Z is negative when the raw score is below the mean and positive when above. A threshold of 2 was used to generate a trigger signal that was sent to the MRI, if the event occurred after a refraction period (generally 500-700 ms) after the last event. The z-score approach was sufficiently robust and stable to eliminate errors from variation of signal quality during the experiment. Moreover, the shift of the ROI or the shift of the artery inside the ROI does not modify the output of the algorithm. Additionally, the placing of the ROI is reasonably flexible and the inclusion of more or less grayscale surrounding tissue does not affect the calculated trigger signal. The signal-processing scheme is non-linear and is based on the number of pixels within the ROI qualifying above a threshold value. Additional noise may add extra pixels (that were otherwise below the threshold) or remove pixels (otherwise above the threshold) but statistically the net result is invariant. The effect is similar to median filter denoising. The overall latency of the image processing and triggering was estimated to less than 33 ms, as no processing queue occurred at 30 fps input video data (the maximum rate of images sent by the SVGA even if the US frame rate could be up to 50 fps).

Doppler intensity traces and z-score of the selected signal were recorded with and without the MRI acquisition running for assessment of potential interference (Fig. 2(A)). ECG and Doppler trigger signals were recorded from the subjects inside the MRI over 60 RR cycles to compare visually in 5 subjects. Actual scan time between the methods was compared in all 10 volunteers.

B. Acquisition: Thermal Safety

Experiments to monitor the potential heating of the transducer surface during MR acquisition used an MR-compatible fluoroptic temperature sensor (STF-5, 5 m long, Luxtron, Santa Clara, CA, USA) connected to a fluoroptic thermometry system (FOT LabKit, Luxtron) placed outside the MR room (supplementary data C).

C. Acquisition: MR Imaging

The 3T MRI protocol consisted of 2- and 4-chamber (2C, 4C) and short-axis (SA) trueFISP (True Fast Imaging with Steady-state Precession) cines with echo time and repetition time (TE and TR) of 1.4 and 39.2 ms, respectively, where TR represents temporal resolution. The echo spacing was 3.3 ms, resolution 1.63×1.63 mm^2, slice thickness 6 mm, matrix 208×174, flip angle 40°, SAR = 1.5 W/kg, and bandwidth 960 Hz/pixel. The retrospective gating gave 25 reconstructed cardiac phases. Aortic phase contrast (PC) flow FLASH (Fast Low Angle Shot) series with TE/TR 2.5/37.1 ms, echo spacing 4.6 ms, resolution 1.98×1.98 mm^2, slice thickness 6 mm, matrix 192×132, flip angle 20°, SAR = 0.4 W/kg, bandwidth 450 Hz/pixel, retrospective gating, 30 cardiac phases and velocity-encoding sensitivity (venc) 200 cm/s were also acquired. The acquisition time for the two sequences depended on heart rate and therefore the breath-hold duration was 9 RR intervals for the cine acquisition and 24 RR for PC flow. All images were acquired with both ECG (standard detection by the scanner embedded monitor) and Doppler triggering as described above. 'False trigger' images used a simulated cardiac signal longer in duration than the true rhythm. For this, a regular simulated trigger was set to a value at least 20% higher (but no more than 30%) different to the actual ECG measured RR interval. The absolute value of the chosen simulated RR was constant for each volunteer, but different between volunteers. The resulting images were used to compare directly with the ECG gold standard and Doppler trigger images as a representation of poorly gated image. These so called 'false' images are essentially ungated and of non-diagnostic quality. These images were then post-processed with the MOG technique (retrospectively corrected k-space).

MOG was implemented in Matlab (v2014, Mathworks, USA). Oversampled dynamic data were reconstructed iteratively, sorting the data based on a hypothetical ECG waveform, optimizing image metrics. Image entropy was calculated to assess the level of blurring or ghosting artifacts that are a result of incorrect gating. The MOG technique has the advantage of not requiring any modification of the pulse sequences, as is the case for other self-gating techniques, and can be used to correct raw data taken directly from the MRI that can then be reconstructed

to the usual DICOM (Digital Imaging and Communications in Medicine) format. At this time, work in adult cardiac imaging has been limited to validation for the fetal protocol, particularly for flow quantification. Here it was applied to adult volunteers for both flow and cine acquisitions.

To assess stability and feasibility of the Doppler trigger compared to conventional ECG over an acquisition time longer than 10 minutes, four-dimensional flow images were acquired in two healthy volunteers, using a prototype pulse sequence. Cardiac synchronization used the ECG or Doppler signals as described above, together with a crossed-pair navigator that enabled tracking to compensate respiratory motion. The crossed-pair respiratory navigator was set with a 6 mm accept range, 0.6 scaling factor and had an acceptance rate of around 60%. Parameters for the 3D FLASH gradient echo, plus time-resolved flow, were resolution 1.8×1.8 mm^2, slice thickness 3 mm, TE/TR 2.34/34.48 ms, echo spacing 4.4 ms, flip angle 8°, SAR = 0.7 W/kg, bandwidth 790 Hz/pixel, with 24 pseudo-sagittal slices covering the aortic arch and 23 cardiac phases, and acquisition time 10 to 15 minutes depending on breathing pattern. Data were segmented and assessed quantitatively using Siemens '4D Flow Demonstrator' software (version 2.4; Siemens Healthcare, Erlangen, Germany). Quantification was done by automated vessel segmentation with flow parameters calculated at 6 or 7 cross sections in the descending aorta.

The hybrid US and 2D MR imaging session lasted for approximately 45 minutes. The 4D MR flow measurement added approximately 30 minutes. Considering the SAR value of the 4D MR sequence, a temperature increase in soft tissue of maximum 0.18 °C was estimated in the subject, adding a non-significant term to the ultrasound imaging thermal index.

D. Acquisition: Volunteer Study

ECG (gold-standard), Doppler and MOG triggering were compared in 10 healthy volunteers (3 female and 7 male, age 30 ± 6 years, weight 75 ± 11 kg). The subjects' heart rate was monitored during the scanning and a measurement of blood pressure taken off line using standard medical equipment. All subjects had normal resting heart rate (60-75 beats/minute) and were normotensive (range of blood pressure systolic 100-121 and diastolic 62-70 mmHg). All volunteers gave informed consent and the study followed the guidelines of the ethical committee of the University Hospitals of Geneva.

E. Imaging Analysis: Image Quality – Scoring

Image quality was scored in a blinded fashion by two experienced radiologists for the two triggering methods, the false trigger and the MOG reconstruction. Montages of cine series, randomized with respect to triggering method, showing 4-chamber, 2-chamber and short-axis images were scored on a scale of 0-3. A single score was given for each method for each subject looking at the 3 classical image planes simultaneously but without knowledge of the triggering method. A score of 3 indicated excellent image quality; 2, good image quality; 1 sufficient image quality and 0, limited diagnostic potential. Statistical differences between methods and inter-observer correlation are reported (SPSS software version 21).

F. Imaging Analysis: Laplacian Sharpness Quantification

Edge gradient sharpness was quantified on septal regions throughout the cycle on Modulus/Laplacian/Median image transforms, which gave positive scaled pixel intensity based on edge gradients. The images were transformed using a gradient quantification based on intensity after applying median, modulus and 3×3 Laplacian transform (1 1 1; 1 −8 1; 1 1 1) to the magnitude images. An ROI on the septum in 4C and SA images was quantified throughout the cardiac cycle with values on the native Laplacian in m^{-2}, measured as a pixel intensity integral and in arbitrary units normalized to the value of the first phase ECG image (in diastole immediately after the R wave) taking this integral to be '1'. ROIs were kept constant within each subject, but were not transferable intersubject, hence the normalization.

G. Imaging Analysis: Ejection Fractions

Left-ventricular area contraction curves where segmented over the whole cycle for both 4C and SA views. Ejection Fraction (EF) was calculated using the biplane method on 4-chamber and 2-chamber views using Osirix (Open source http://www.osirix-viewer.com/). The endocardial contour was delineated manually for systolic and diastolic phases, for each slice of the myocardium, to calculate volumes with EDV defined as the end-diastolic volume and ESV the end-systolic volume. EF (%) was defined as $100 \times$ (EDV-ESV)/EDV.

H. Imaging Analysis: Peak Velocity and Flow

Flow velocity was calculated from the phase contrast images using the Osirix plug-in for 'ROI enhancement'. The peak velocity and flow in each location were compared.

I. Imaging Analysis: Statistical Analysis

ANOVA (Bonferroni, with SPSS software version 21) was used to compare results from the different trigger methods. Statistically significant differences are defined as $p < 0.05$.

III. Results

A. Doppler Set-Up and Image Data

Maintaining placement of the probe was successful and comfortable for the subject in all cases. Positioning the probe took 5-10 minutes (improving with experience). MR imaging was completely free of any potential interferences generated by US. Detectable but non-significant artifacts were observed on pulsed color Doppler during MR acquisition. Physically, increasing the pulsed color Doppler velocity-encoding range and reducing the power of emitted pulses alleviated the perturbations. Numerically, adjustment of z-score threshold for triggering suppressed all interference from MR acquisition on the logical output signal for each subject. Fig. 2(B), with arrows indicating the negligible artifacts from MRI, shows the recorded Doppler with and

TABLE I
QUANTIFICATION OF NOISE LEVEL ON DOPPLER

	without MRI	with MRI
Mean baseline 'signal'	3446 (+−310)	3396 (+−329)
R wave peak	7299	7540
SNR at R wave peak	42	27
Baseline noise	170 (+−83)	277(+−107)

Quantification of noise level on Doppler inside the MRI with and without MRI sequence running of the R-wave peak as well as the positive signal between R-waves and the noise in the 'negative' Doppler band.

without MRI running (see also supplementary video A) and the output to the MRI. The latter shows no change in trigger efficiency in the two cases. The average time between data points was 61 ms, leading to a frame rate of 16/s. Doppler curves were acquired over more than 10 minutes (see Fig. 2 shows an illustration of part of this time period). The autocorrelation is very high with only 5 missed triggers observed and counted over the 10 minutes acquisition (data not shown). In another test with MRI running and Doppler detection, the average heart period over this acquisition time in a single simultaneous acquisition was 929 ms for ECG and 925 ms for Doppler with a variation of the mean sd (as a % of heart rate) of $<1\%$ for both methods (maximum variation of 1.2% for ECG and 1.5% for Doppler). In addition, the noise level on the Doppler signal with and without MRI was quantified over the R-wave period that would be used for the trigger and in the baseline noise. SNR was defined as the peak signal amplitude divided by the mean of the background noise (negative portion of US signal). The baseline signal is the positive US signal between R waves. A frame of a recorded movie = 8 RR (approximately the same duration as the breathold cine acquisitions) was converted to grayscale giving the results in Table I showing excellent Doppler SNR for peak detection with or without MRI acquisition running.

B. Trigger Efficiency

Flow image duration was 24 cardiac cycles; this was the longer than the cine images (9 RR) and was the most intense in terms of gradients (and consequent potential for interference). The acquisition times were not significantly different between the ECG and Doppler triggering methods, meaning the efficiency was equal. Over the 10 volunteers the acquisition times were ECG 21.31 ± 2.45 s and Doppler 21.75 ± 2.12 s with no significant difference in paired t test, $p = 0.07$. There was no significant difference in ANOVA between ECG and Doppler triggered acquisition time, $p = 0.67$ and the acquisition times correlated with $R^2 = 0.93$ ($y = 1.11 \times 2.97$) as shown in Fig. 3.

Visual recording of the MRI interface of ECG and Doppler trigger in the MRI machine for 5 volunteers was done with each plot covering 6 blocks of 12 RR intervals. This is longer than both the cine and flow acquisition times. Graphs were analyzed for the signal detection in the Doppler algorithm. No pulses were missed and the start of Doppler was a consistent time delay in the range 360 - 480 ms (subject dependent) after the R wave in each case. False triggers were set a fixed value, but not equal to the true RR.

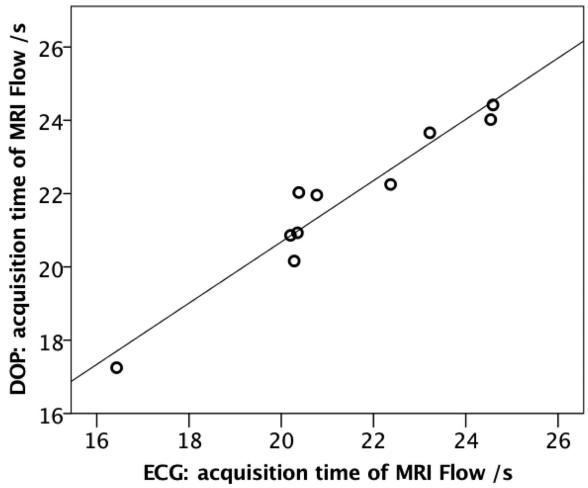

Fig. 3. Actual acquisition times (in seconds) for the flow MRI for the Doppler and ECG trigger methods in all volunteers, showing no difference and an excellent correlation. For the 24 cardiac cycle acquisition there was no significant difference in time, showing equal efficiency of the two triggering methods).

C. Robustness to Motion

The robustness to motion was illustrated in one volunteer with significant carotid motion during respiration. The supplementary movie B shows a recording of the Doppler signal and Fig. 4 shows the regularity of the intensity algorithm and generated signal with selected frames from the movie. Also, the advantage of spatially resolved Doppler over a single source, was that the region placed avoids signal from the jugular, which was also present in the full US FOV, and could potentially contaminate the signal. Fig. 4(C) shows the calculation of intensity over the whole region showing the contamination that would result from a non-spatially resolved Doppler. This whole FOV signal did not send a successful trigger to the MRI.

D. Thermal Safety

In experiments to monitor the potential heating of the front side of the probe during MR acquisition, an MR-compatible fluoroptic temperature sensor (supplementary data C), demonstrated that no heating effect was detected within the precision and accuracy of the fluoroptic thermometer (STD = 0.059 °C over 300 sec acquisition).

E. MR Image Quality - Scoring

Fig. 5(A) shows image quality of the 4-Chamber and Short Axis cine frames (see also supplementary video D). High-resolution cine imaging was also possible and is shown along with normal resolution for Doppler- and ECG-triggered imaging (Fig. 5(B)). The visual image quality for the MOG reconstruction is poorer than the ECG and Doppler triggers, as illustrated by the scoring, but accurate functional parameters could be measured and the images were deemed of diagnostic quality.

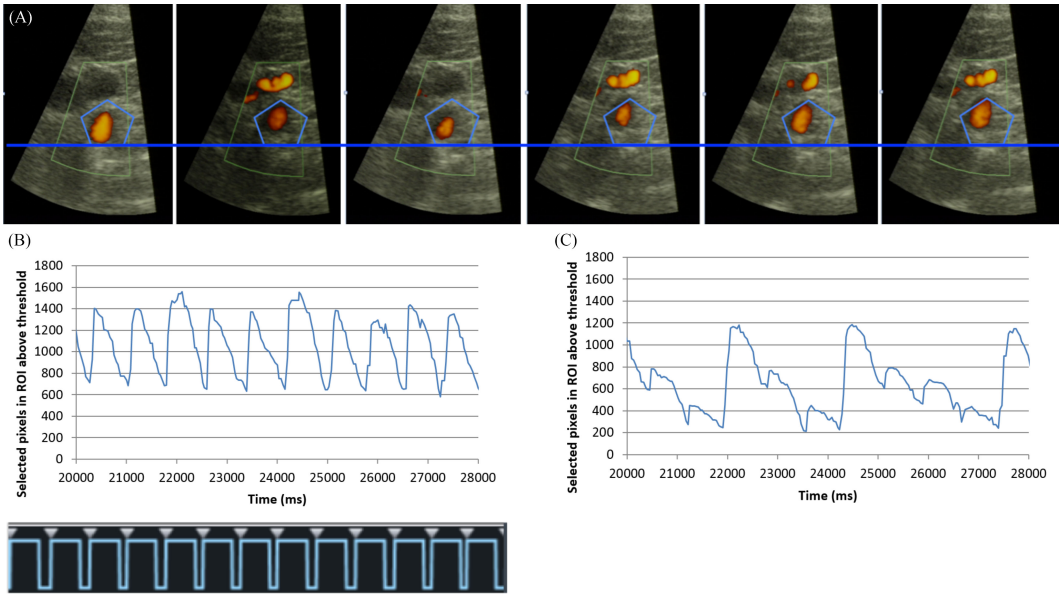

Fig. 4. (A) Timeframes of the Doppler signal in a volunteer with significant motion during the acquisition. (B) The intensity calculation from the algorithm and the resulting trigger signal. (C) The algorithm output from a large region illustrating contamination from the jugular when the Doppler is not spatially resolved.

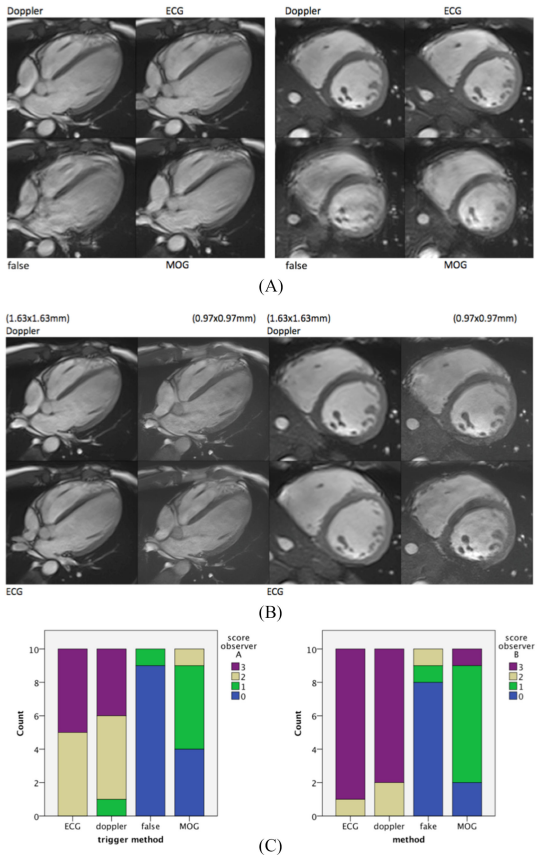

Fig. 5. (A) Breath-hold 4-chamber and short-axis MRI images of the heart (single frame from 25/RR) using Doppler-, ECG-, false-trigger and MOG. Septum blurring was evident under poor gating conditions (false trigger) but there was comparable sharpness in other methods. (B) Normal (1.63×1.63 mm^2) and high-resolution (0.97×0.97 mm^2) Doppler- and ECG-triggered cine frames. (C) Histogram of scoring of image quality by two observers (0-3) based on 4-chamber, 2-chamber and short-axis images combined.

TABLE II
QUALITATIVE SCORING OF IMAGE QUALITY BY TWO INDEPENDENT, EXPERT OBSERVERS

	observer A score (n = 10) mean ± s.d.	observer B score (n = 10) mean ± s.d.	All scores (A & B) (n = 20) mean ± s.d.
ECG	2.50 ± 0.53	2.90 ± 0.32	2.70 ± 0.47
Doppler	2.30 ± 0.67	2.80 ± 0.42	2.55 ± 0.60
False	0.10 ± 0.32	0.30 ± 0.67	0.20 ± 0.52
MOG	0.70 ± 0.67	1.00 ± 0.82	0.85 ± 0.74

Table II and Fig. 5(C) show the mean scores from 2 expert readers. Intra-class correlation between readers was 0.95 for averaged measures and 0.91 for single measures. Both observers (and the scores from the two combined) showed no significant difference between Doppler- and ECG trigger ($p = 1.00$), but a significant difference to false triggering ($p < 0.0005$). Due to the larger variation in scores for the MOG reconstruction (between subjects), the scores for this method were lower than Doppler- and ECG trigger, but still higher than the false trigger image for each observer ($p = 0.07$). Nevertheless, as described below, functional measurements were in agreement with the triggered images.

F. Laplacian Sharpness Quantification

Fig. 6 shows Modulus/Laplacian/Median filtered images and the corresponding magnitude images. Quantification of the septum for SA and 4C for 10 subjects (n = 20) showed 8 cases where Doppler-triggered images had higher values for mean 'sharpness' than ECG. For the cases where Doppler was sharper, the normalized quantification was 1.27 ± 0.21 for Doppler and 1.10 ± 0.09 for ECG which showed a larger difference than

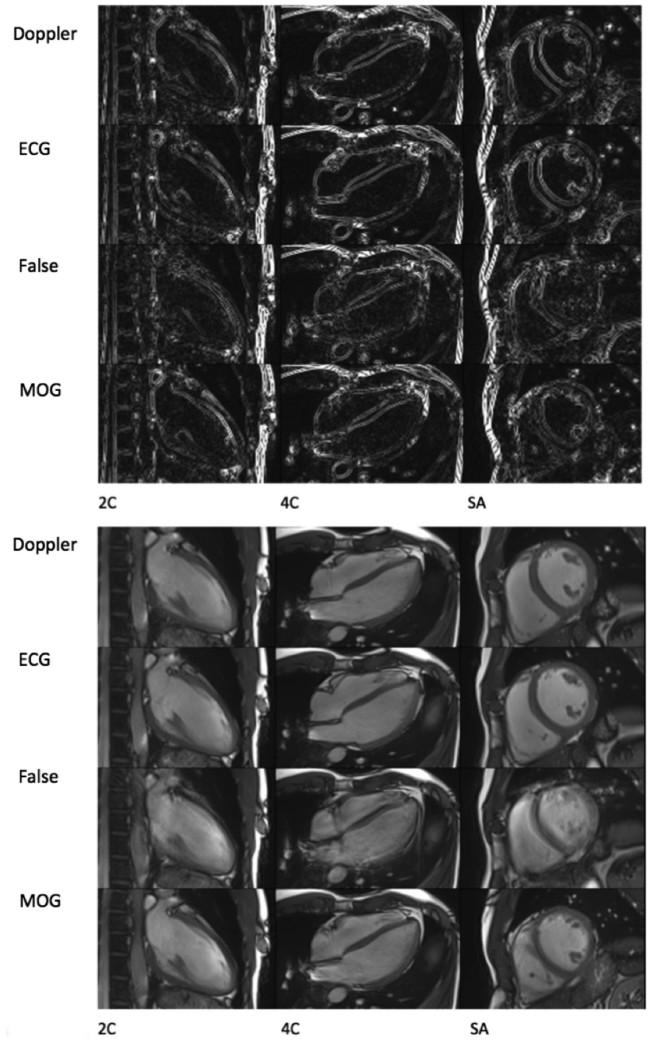

Fig. 6. Median and Laplacian transformation of images showing edge sharpness. Normal magnitude images showing sharpness in the diastolic phase.

TABLE III
SHARPNESS QUANTIFICATION

	4C mean ± s.d.	SA mean ± s.d.
ECG	1.09 ± 0.15	1.04 ± 0.21
Doppler	1.11 ± 0.26	1.04 ± 0.25
False	0.98 ± 0.22	0.98 ± 0.24
MOG	1.02 ± 0.17	0.95 ± 0.27

Normalized to ECG first phase normalized integral intensity (from native Laplacian images with units of m^{-2}).

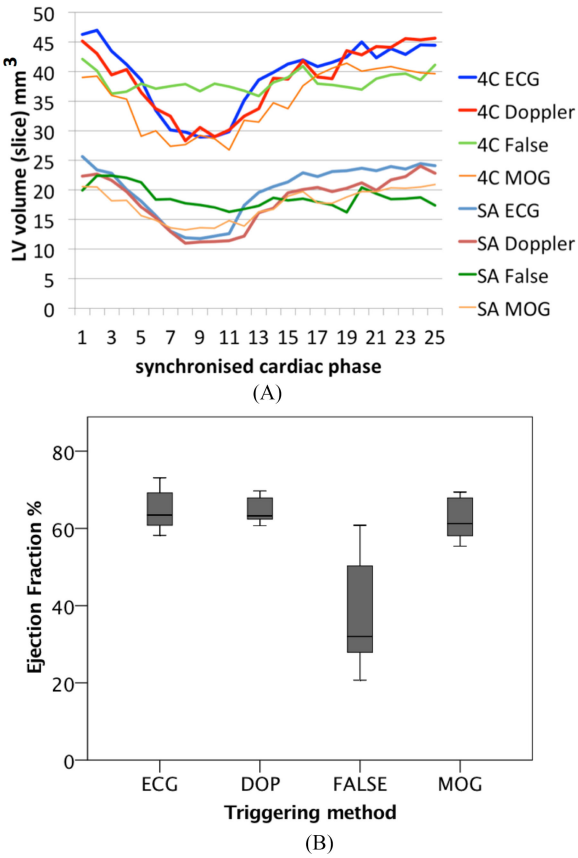

Fig. 7. (A) LV contraction curves for 4-chamber (4C) and short axis (SA) slice volume showing the full cardiac cycle for each method, and (B) Ejection fractions (%) for the ECG, Doppler, false trigger and MOG methods. Significant difference was only seen with false trigger $p < 0.05$.

the cases where ECG was better (0.94 ± 0.09 for Doppler and 1.04 ± 0.13 for ECG). When divided into groups of one modality being better than the other, there was a significant difference between Doppler and ECG, with $p = 0.047$ when Doppler was sharper and 0.042 when ECG was sharper. However, overall, there was no significant difference between ECG- and Doppler trigger by ANOVA ($p = 1.00$) showing statistically both performed equally well. There was a significant difference to the false trigger and MOG ($p < 0.05$). Table III shows mean and standard deviation sharpness quantification (Laplacian total intensity in septum region normalized to the first phase of the ECG-triggered image).

G. Function and Ejection Fraction (ECG-, Doppler-Trigger, MOG, FALSE)

Plotting LV (left ventricular) area contraction curves over the whole cycle for SA and 4C showed no difference between ECG and Doppler (example shown in Fig. 7(A)). False trigger gave incorrect function, clearly visible on these curves. Mean difference between contraction curves for the 4C derived from the different triggered acquisitions (all subjects and phases, with mean LV area of 34 mm^2, range 19-46 mm^2) was 1.67 ± 0.29 for ECG:Doppler ($p = 0.58$), 3.73 ± 1.05 for false:ECG ($p = 0.96$), 3.30 ± 1.14 for false:Doppler ($p = 0.50$), 3.10 ± 0.62 for ECG:MOG, 2.76 ± 1.17 for false:MOG and 2.76 ± 0.92 for Doppler:MOG, with ICC > 0.85 for ECG, Doppler and MOG. T-test shows none of these differences were significant ($p > 0.10$, except for ECG:false $p = 0.048$). This shows good agreement between the methods over the whole cycle and the smallest difference for ECG:Doppler (significantly smaller than the other difference pairs with $p < 0.015$).

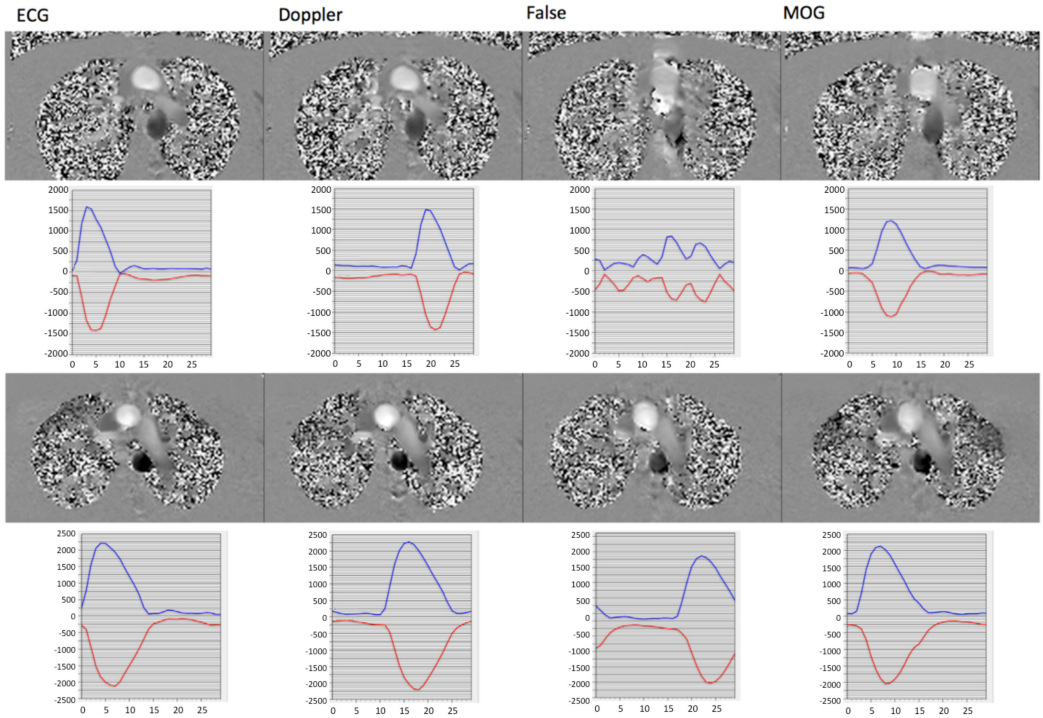

Fig. 8. Flow profiles in ascending and descending aorta in two subjects, one with very poor trigger due to 'false trigger' and the second where the flow was only compromised in terms of peak value and not profile.

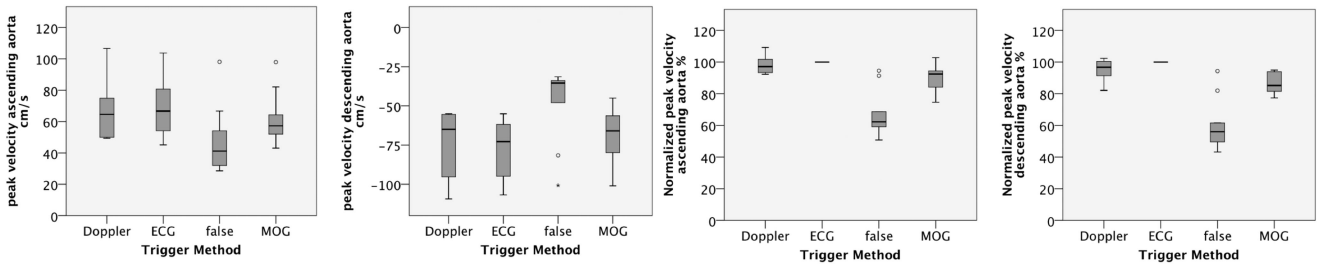

Fig. 9. Peak velocity in the ascending and descending aorta: absolute values in cm/s and normalized to ECG (%). False trigger is significantly different to the three statistically equivalent triggered methods.

Visibly, ejection fraction showed no difference between ECG- and Doppler triggering with equally good function calculation from both methods. False trigger gave incorrect function, but MOG succeeded in recuperating correct values for EF (Fig. 7(B)). Statistically, ECG-, Doppler-trigger and MOG ejection fractions were equivalent ($p = 1.00$), despite the perceived lower image quality for MOG, with those derived from false trigger much more variable and significantly lower ($p < 0.0005$). Mean values (%) were ECG 64.73 ± 5.30, Doppler 64.50 ± 3.06, MOG 62.22 ± 5.31, and false 38.92 ± 14.94.

H. Peak Velocity and Flow

ECG- and Doppler-triggered flow showed a higher peak velocity than false-triggered images, which in some cases showed several peaks per cycle (Fig. 8) or simply a reduced peak value. The peak velocity (Fig. 9) in the ascending and descending aorta was not different between ECG and Doppler ($p = 0.31$ for ascending and 0.06 for descending) by paired t-test. False trigger showed difference to Doppler- and ECG-trigger peak flow in the descending aorta ($p = 0.04$ for Doppler and 0.02 for ECG), but otherwise all 3 methods (with MOG) were not significantly different ($p > 0.05$). The quality of the flow images for the 'false trigger' was very variable. If the false trigger was not too far from reality, the visual shape of the flow profiles and images could be consistent with reality. However, on quantification of flow a discrepancy (reduction) in peak velocity values was observed despite a good flow profile. Others had completely mixed velocity profiles with several peaks and would not be quantifiable for true peak flow. This variability did not affect the MOG reconstruction, but did lower the statistical difference between false trigger and the other methods. Normalizing to the 'gold-standard' ECG (Fig. 9), to reduce the variability between subjects, excellent agreement was obtained between the ECG- and Doppler-triggered images and MOG ($0.09 < p < 1.00$) with all having a difference to false-triggered images ($p < 0.001$).

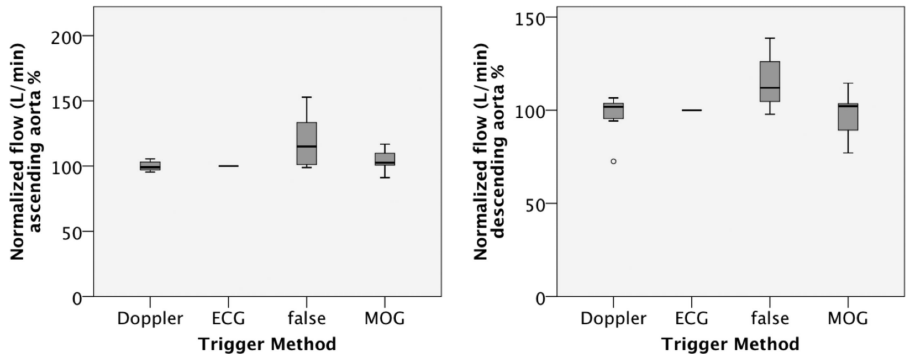

Fig. 10. Flow in the ascending and descending aorta (normalized to ECG). False trigger is significantly different to the three statistically equivalent triggered methods.

Flow (L/min) in the ascending and descending aorta were not significantly different between ECG- and Doppler-triggered images and MOG ($p > 0.54$), though due to the large variation between volunteers, the values for the false trigger were also not significantly different. In the case of flow, values from normal volunteers can show an even wider variation than peak velocity so therefore these values were also normalized to the 'gold-standard' ECG value. In this case (Fig. 10), the ECG- and Doppler-triggered images and MOG showed no significant difference ($p = 1.00$) and all three were different to the false-triggered results ($0.002 < p < 0.04$) for both the ascending and descending aorta. The time shift between the triggering methods also meant that the start of the upslope is most clearly visible on the Doppler-triggered image.

I. 4D Flow

Images showing 3 directional phase images, segmentation and flow parameters are given in Fig. 11. Moving reconstructions are presented in supplementary data (videos E & F). The comparison of the two trigger methods illustrated Doppler triggering feasibility even for very long complex cardiac MR acquisitions. Fig. 11 illustrates 4D flow from the two triggering methods over 6 or 7 vessel cross sections. In these two illustrative cases, the peak phase in the Doppler-triggered image was around 10% different and peak flow in various cross sections of the aorta between 3 and 9% smaller for Doppler. A larger dispersion of velocity is observed using Doppler triggering, than with ECG as small spatio-temporal inaccuracies may accumulate. This will be the focus of future work.

IV. Discussion

In this paper, we describe new developments in biomedical engineering enabling the use of MR-compatible color pulsed Doppler, which was achieved with 1) specially shielded US probe positioned in direct contact to the skin and 2) efficient signal conversion using a spatial integral and temporal standard score to detect the peak onset. We used clinical standard devices producing interference-free MR images acquiring state-of-the art clinical protocols for cardiac MRI. Typically, this included morphological and functional "cine" acquisitions and phase contrast flow.

The new technology allowed cross-compatible images, most importantly the echo Doppler did not show significant vibrations of the US imaging probe. For comparison, in the most recent paper [4], a system that allowed simultaneous acquisition of MR and US images was developed. B-mode and Doppler US in that paper were performed inside the bore of a clinical 1.5 T MRI scanner using a clinical 1–4 MHz US transducer with an 8 m long cable. However, susceptibility artifacts and RF noise were introduced into MR images by the US imaging system [4]. These artifacts were minimized by foil wrapping of the cable and maintaining a 4 cm gap between the phantom and probe. Acoustic noise and/or vibration artifacts were also seen on the Doppler during MR acquisition.

Previous studies have compared triggering methods, but without spatially resolved Doppler that allows extension of the method to real-time slice tracking and to cases where no ECG signal is available [13], [27], [28]. The potential interest of Doppler signal as an alternative trigger to ECG in cardiac MR imaging has been suggested recently by Kording *et al*. [27], who demonstrated the technical feasibility using a transmit-receive, single-element US transducer and an effective sampling rate of 200 Hz. To the best of our knowledge, spatially resolved Doppler acquired by a clinical ultrasound scanner has not been previously reported for triggering cardiac MRI. The proposed method was insensitive to local motion as the Doppler signal is integrated inside an encompassing user-defined ROI. It has the advantage of targeting a precise source of Doppler signal in a single vessel, thus avoiding mixing of opposite flow directions, or of arterial and venous signals, that have different hemodynamic features and peak flow times, hindering the flow curve as shown in Fig. 4(C).

The proposed method in this paper is independent of the MR scanner and sequence protocol. Direct comparison between velocity measurements by US Doppler and PC MR was beyond the purpose of the study, but is suggested to be feasible under conditions of a sufficient acoustic window to the respective blood vessel.

Conversely, an active compatibility of the two devices is more difficult to achieve for the proposed setup, and the temporal resolution of Doppler signal is significantly lower. While our ultrasound scanner could work in pulsed color Doppler mode at a frame rate of up to 50 Hz, the data transfer was limited

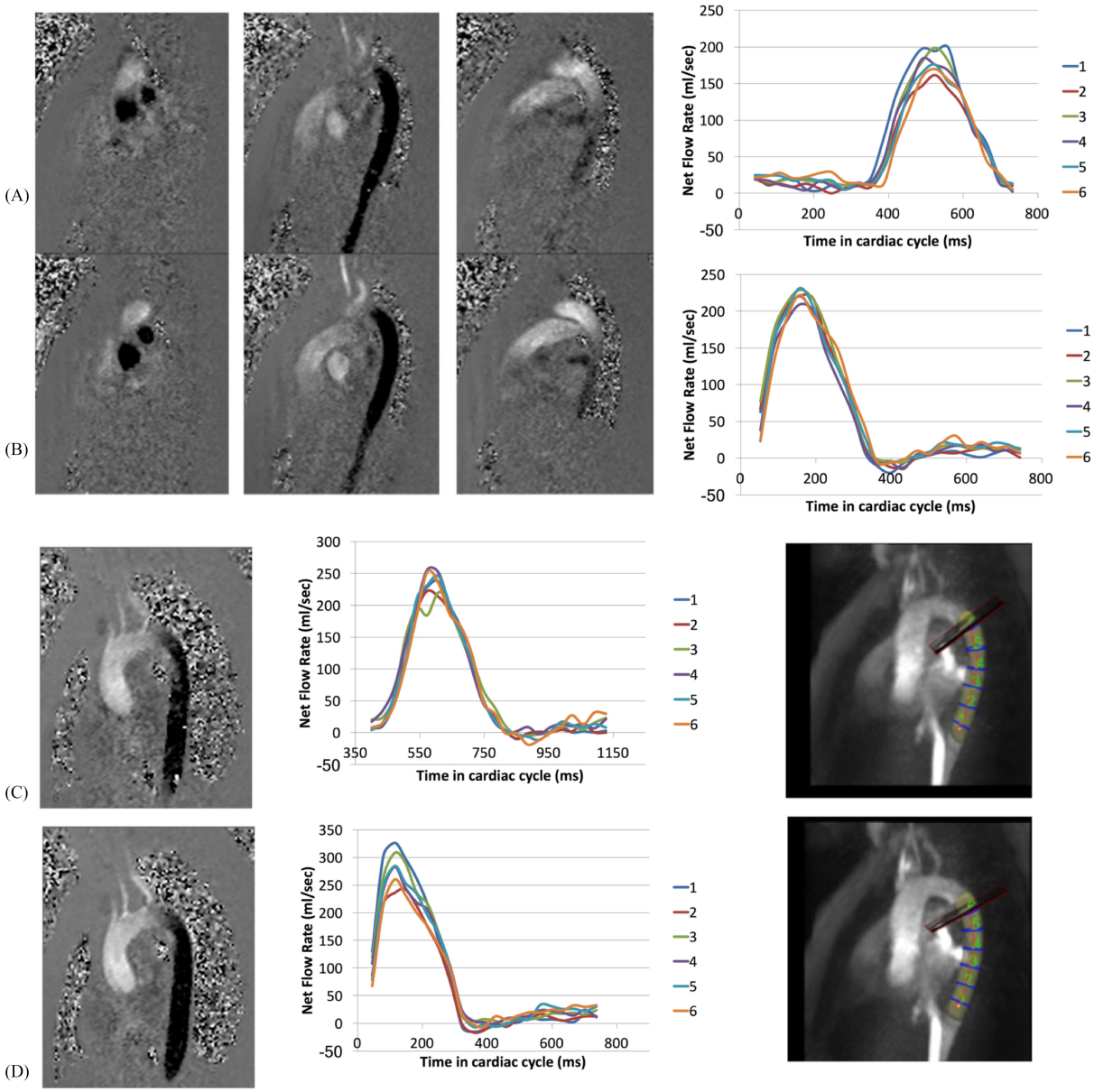

Fig. 11. 4D flow phase images (3 directions) with Doppler (A) and ECG (B) triggering with corresponding plots of net flow rate for the two methods. Vertical encoding direction from a second subject with Doppler (C) and ECG (D) triggering and net flow rate plots along with an illustration of segmentation of descending aorta with 6 cross section locations for flow quantification. The colored curves represent the segmented cross sections (illustrated bottom right), with Section I being the most distal, and 6 being the proximal.

to 30 Hz. In addition, processing 2D color images is more computer-intensive than for 1D signals, potentially inducing a time delay between acquisition and trigger output. However, a constant time delay would still not influence the retrospective cine MR acquisition as only a synchronous trigger is required, and in any case the Doppler trigger is already shifted with respect to the ECG. In the current study, only healthy adult volunteers were enrolled, and the resting state cardiac cycle duration was longer than 800 ms in all cases. The frame rate of the ultrasound imaging and data transfer was sufficient for the temporal resolution of the cardiac function images. Subsequently, the image quality and cardiac function parameters were clearly excellent for the proposed method compared to the standard ECG-triggered method. The described setup would require further improvement in data transfer for faster heart rate conditions.

This study was limited to only healthy volunteers, despite the significant clinical potential. It provides useful insights into the technology and opens the way to application in clinical patients. Expert radiologists assessed the volunteer images for the potential diagnostic ability in this routine clinical MR protocol. A limitation of the expert scoring in our study is the visual time difference between the Doppler- and ECG-triggered cardiac-cycle imaging. It is therefore difficult to be truly blinded to the trigger type. However, the Doppler trigger had the added advantage that the peak flow and systolic contraction were in the

middle of the analyzed cycle with a clear baseline both sides, making an upslope of flow or the diastolic volume more easily identified.

One volunteer had significant motion of the artery during acquisition with no adverse effects on the Doppler signal. This shows potential for the application in fetal imagery, where not only do we have no direct access to the ECG, but also the possibility of a moving Doppler signal. According to terHaar [29] and the British Medical Ultrasound Society guidelines [30] for obstetric and neonatal transcranial scanning, ultrasound scanning time is restricted for any TI value greater than 0.7. Considering for instance the TI value of 0.8 estimated for our study using color Doppler and B-mode background and targeting a carotid artery at a few centimeters depth, the duration should not exceed one hour. This interval is the standard and sufficient to conduct a clinical MRI examination. Moreover, the central frequency of US imaging for obstetric would be lower than the value used (7 MHz), yielding a lower thermal index.

There also exist some time sampling limitations, which can be improved in the near future with the evolution of the technology. The narrower the angular sector to be swept by the ultrasound beam, the higher the available rate, meaning that deeper targets can be scanned faster. In our study the common carotid artery was a rather superficial target requesting a larger angular sector. The 16 Hz sampling rate yields a maximum temporal uncertainty of half the dwell time, that is ± 31 ms and an average temporal uncertainty of ± 16 ms. As the duration of the cardiac cycle is not an integer multiple of the sampling period, the rounding errors were distributed across the "cine" acquisition potentially yielding additional blurring. This has a stronger potential impact at higher cardiac frequency. However, the flow curve in the aorta or in large arteries such as the carotid is smoother and broader than the ECG signal (particularly the QRS wave) because of the convolution with the cardiovascular mechanical response function. In other words, the trigger method is not sampling the same phenomenon. As far as we are able to localize the maximum flow signal peak during one cardiac signal this should suffice as a trigger reference. Localizing the time point of maximum signal could also be improved using numerical filtering or modeling, which will be addressed in future studies.

With regard to the cardiac cycle seen with ECG, Doppler and eventually pulse oxymetry, the flow rate profile in the carotid is more adapted to peak detection by Doppler than the peripheral vessels and even the aorta with regard to upslope [31]. A pulse oxymeter tends to have no flat 'baseline' period and a relatively symmetric upslope and downslope. The carotid Doppler signal has a sharp upslope where our integral signal peak is detected. While the Doppler signal has a lower frequency component than ECG, it is still closer to the heart and a sharper peak than pulse oxymetry detected at the fingertip. Another physical method of acoustic gating has been proposed [12], performing better than ECG and pulse oxymetry at high field in terms of reliability and detection variance. However, the method currently necessitates careful coil and gradient coil design and would, like all triggering methods, benefit from wireless transmission technology.

The 4D flow technique is illustrated in two subjects. A 4D flow "full" volunteer study with high statistical power seems beyond the scope of the present manuscript, and will be further investigated in current studies. Unlike cardiac electrical stimulation for ECG, Doppler triggering is based on hydrodynamic phenomena, which are also directly detected by the PC flow-encoding mechanism. For instance, a regularization algorithm can be easily implemented to skip the cine MR data acquired in the cardiac cycles when the peak flow is fluctuating outside a predefined range. The ECG electrical signal merely sends a trigger and does not assess the difference in flow or contraction that could contaminate the averaged data in an acquisition if a cycle with different hemodynamics is included. The use of fluid mechanical properties rather than electrical signal gave coherence to using the 3D spatial Doppler to control the 3-directional temporal flow data of the '4D' technique. The same 3D fluid dynamics affect the Doppler signal and produce the 4D flow patterns, therefore perhaps being more physically relevant than using electrical stimulation.

The advances in technology providing MR-compatible [32] and portable ultrasound devices [33] mean that the applications of such techniques could be translated into the clinical setting. However, using spatially resolved pulsed color Doppler imaging has the fundamental advantage to enable the operator to choose the spatial source of the signal, e.g., arterial flow alone. Importantly, our 2D flow detection algorithm is insensitive to the in-plane local motion of the signal source, unlike a one-ray scanning using a 1D US transducer within a moving environment [14]. With respect to the fetal MR imaging goal, through-plane motion is expected to be a significant challenge, requesting time effective repositioning of the probe and completion of MR data acquisition before new motion occurs. An early pregnancy stage would be easier to manage than a late one. In our approach, the Doppler ultrasound information is requested to generate a trigger signal, not for quantitative flow diagnostic. The ALARA principle [34] should be applied as the minimum mechanical and thermal index of Doppler ultrasound still permitting a stable triggering, which is less resource demanding than quantitative flow diagnostic.

Furthermore, our technology has other potential applications, for instance improved motion tracking in the abdomen for focused ultrasound. Unlike B-mode or harmonic imaging of back-scattered ultrasound signal, pulsed color Doppler has a significantly higher contrast-to-noise ratio due to blood flow in the vessels and is more robust for motion tracking. This includes a higher tolerance to out-of-plane motion than for speckle tracking, especially when the blood vessel is nearly perpendicular to the imaging plane.

V. Conclusion

Phase Contrast flow and cine images were successfully obtained in healthy volunteers with ECG triggering, Doppler triggering, and MOG post processing. Image quality was highly comparable and accurate functional parameters were accessible, with quantitative images obtained with the proposed Doppler ultrasound triggering for MRI.

This quantitative study has focused on breath-hold images with Doppler used for cardiac triggering, with the addition of the feasibility of the longer respiratory-navigated 4D flow. However, the hardware platform is designed to further enable advanced cardiac imaging using real-time slice tracking locking imaging planes to respiratory and/or cardiac motion under free breathing. This will provide increased patient comfort with motion correction during longer total scan times as well as the potential for cardiac studies in patients where the ECG is unavailable. This method, therefore, opens up the clinical applications of high-resolution valve tracking and fetal cardiac MRI.

References

[1] M. Gunther and D. A. Feinberg, "Ultrasound-guided MRI: preliminary results using a motion phantom," *Magn. Reson. Med.*, vol. 52, no. 1, pp. 27–32, Jul. 2004.

[2] B. D. de Senneville *et al.*, "Real-time adaptive methods for treatment of mobile organs by MRI-controlled high-intensity focused ultrasound," *Magn. Reson. Med.*, vol. 57, no. 2, pp. 319–330, Feb. 2007.

[3] C. Chandrana *et al.*, "Development of a platform for co-registered ultrasound and MR contrast imaging in vivo," *Phys. Med. Biol.*, vol. 56, no. 3, pp. 861–877, Feb. 2011.

[4] V. Sherwood *et al.*, "Development of a hybrid magnetic resonance and ultrasound imaging system," *Biomed. Res. Int.*, vol. 2014, 2014, Art. no. 914347.

[5] L. Petrusca *et al.*, "Hybrid ultrasound/magnetic resonance simultaneous acquisition and image fusion for motion monitoring in the upper abdomen," *Invest Radiol.*, vol. 48, no. 5, pp. 333–340, May 2013.

[6] A. M. Tang *et al.*, "Simultaneous ultrasound and MRI system for breast biopsy: Compatibility assessment and demonstration in a dual modality phantom," *IEEE Trans. Med. Imag.*, vol. 27, no. 2, pp. 247–254, Feb. 2008.

[7] C. W. Roy *et al.*, "Accelerated MRI of the fetal heart using compressed sensing and metric optimized gating," *Magn. Reson. Med.*, vol. 77, no. 6, pp. 2125–2135, Jun. 2017.

[8] B. P. Schoennagel *et al.*, "Fetal blood flow velocimetry by phase-contrast MRI using a new triggering method and comparison with Doppler ultrasound in a sheep model: A pilot study," *Magn. Reson. Mater. Phys. Biol. Med.*, vol. 27, no. 3, pp. 237–244, Jun. 2014.

[9] S. Z. Dong and M. Zhu, "Utility of fetal cardiac magnetic resonance imaging to assess fetuses with right aortic arch and right ductus arteriosus," *J. Maternal Fetal Neonatal Med.*, vol. 7, pp. 1–5, May 2017.

[10] S. Z. Dong and M. Zhu, "Magnetic resonance imaging of fetal persistent left superior vena cava," *Sci. Rep.*, vol. 7, no. 1, Jun. 2017, Art. no. 4176.

[11] J. A. Kailin *et al.*, "Fetal left-sided cardiac structural dimensions in left-sided congenital diaphragmatic hernia - association with severity and impact on postnatal outcomes," *Prenat Diagn*, vol. 37, no. 5, pp. 502–509, May 2017.

[12] T. Frauenrath *et al.*, "Acoustic cardiac triggering: A practical solution for synchronization and gating of cardiovascular magnetic resonance at 7 Tesla," *J. Cardiovascular Magn. Reson.*, vol. 12, 2010, Art. no. 67.

[13] D. A. Feinberg *et al.*, "Hybrid ultrasound MRI for improved cardiac imaging and real-time respiration control," *Magn. Reson. Med.*, vol. 63, no. 2, pp. 290–296, Feb. 2010.

[14] J. M. Rubin *et al.*, "Doppler US gating of cardiac MR imaging," *Acad. Radiol.*, vol. 7, no. 12, pp. 1116–1122, Dec. 2000.

[15] D. Piccini *et al.*, "Respiratory self-navigated postcontrast whole-heart coronary MR angiography: Initial experience in patients," *Radiology*, vol. 270, no. 2, pp. 378–386, Feb. 2014.

[16] M. Renker *et al.*, "A non-contrast self-navigated 3-dimensional MR technique for aortic root and vascular access route assessment in the context of transcatheter aortic valve replacement: Proof of concept," *Eur. Radiol.*, vol. 26, no. 4, pp. 951–958, Apr. 2016.

[17] S. Coppo *et al.*, "Free-running 4D whole-heart self-navigated golden angle MRI: Initial results," *Magn. Reson. Med.*, vol. 74, no. 5, pp. 1306–1316, Nov. 2015.

[18] D. Piccini *et al.*, "Respiratory self-navigation for whole-heart bright-blood coronary MRI: Methods for robust isolation and automatic segmentation of the blood pool," *Magn. Reson. Med.*, vol. 68, no. 2, pp. 571–579, Aug. 2012.

[19] L. Feng *et al.*, "XD-GRASP: Golden-angle radial MRI with reconstruction of extra motion-state dimensions using compressed sensing," *Magn. Reson. Med.*, vol. 75, no. 2, pp. 775–788, Feb. 2016.

[20] J. F. van Amerom *et al.*, "Fetal cardiac cine imaging using highly accelerated dynamic MRI with retrospective motion correction and outlier rejection," *Magn. Reson. Med.*, Apr. 2017, doi: 10.1002/mrm.26686.

[21] M. S. Jansz *et al.*, "Metric optimized gating for fetal cardiac MRI," *Magn. Reson. Med.*, vol. 64, no. 5, pp. 1304–1314, Nov. 2010.

[22] C. W. Roy *et al.*, "Dynamic imaging of the fetal heart using metric optimized gating," *Magn. Reson. Med.*, vol. 70, no. 6, pp. 1598–1607, Dec. 2013.

[23] M. Seed *et al.*, "Feasibility of quantification of the distribution of blood flow in the normal human fetal circulation using CMR: A cross-sectional study," *J. Cardiovascular Magn. Reson.*, vol. 14, pp. 78–89, 2012.

[24] M. Markl *et al.*, "Comprehensive 4D velocity mapping of the heart and great vessels by cardiovascular magnetic resonance," *J. Cardiovascular Magn. Reson.*, vol. 13, pp. 7–28, 2011.

[25] M. Markl *et al.*, "Time-resolved 3D MR velocity mapping at 3T: Improved navigator-gated assessment of vascular anatomy and blood flow," *J. Magn. Reson. Imag.*, vol. 25, no. 4, pp. 824–831, Apr. 2007.

[26] R. J. Larson and M. J. Mary, *An Introduction to Mathematical Statistics and its Applications*, 3rd ed. London, U.K.: Pearson, 2000.

[27] F. Kording *et al.*, "Doppler ultrasound compared with electrocardiogram and pulse oximetry cardiac triggering: A pilot study," *Magn. Reson. Med.*, vol. 74, no. 5, pp. 1257–1265, Nov. 2015.

[28] G. Liu *et al.*, "Ultrasound-guided identification of cardiac imaging windows," *Med. Phys.*, vol. 39, no. 6, pp. 3009–3018, Jun. 2012.

[29] G. R. ter Haar, *The Safe Use of Ultrasound in Diagnosis*, 3rd ed. London, U.K.: British Inst. Radiol., 2012.

[30] BMUS, 2009. [Online]. Available: https://www.bmus.org/static/uploads/resources/BMUS-Safety-Guidelines-2009-revision-FINAL-Nov-2009.pdf. Accessed 2017.

[31] P. Reymond *et al.*, "Validation of a one-dimensional model of the systemic arterial tree," *Amer. J. Physiol. Heart Circ Physiol.*, vol. 297, no. 1, pp. H208–H222, Jul. 2009.

[32] D. Speicher *et al.*, "MRI compatible ultrasound transducers for simultaneous acquisition of coregistered ultrasound to MRI data," *Phys. Procedia*, vol. 70, pp. 1002–1006, 2015.

[33] L. Tina and K. M. Johan, "An inventory of current available ultrasound devices for dental use," *Open Dent J.*, vol. 9, pp. 319–329, 2015.

[34] Z. Hlinomazova and I. Hrazdira, "ALARA principle and safety problems of diagnostic ultrasound," *Scripta Medica (BRNO)*, vol. 78, no. 6, pp. 341–346, 2005.